

Anomalous Hall and Nernst effects in ferrimagnetic Mn₄N films: Possible interpretations and prospects for enhancement

Shinji Isogami^{1*}, Keisuke Masuda¹, Yoshio Miura¹, Rajamanickam Nagalingam¹, and Yuya Sakuraba^{1,2}

¹ Research Center for Magnetic and Spintronic Materials, National Institute for Materials Science, Sengen 1-2-1, Tsukuba, Ibaraki 305-0047 Japan

² PRESTO, Japan Science and technology Agency, Saitama 332-0012, Japan

*E-mail: isogami.shinji@nims.go.jp

Ferrimagnetic Mn₄N is a promising material for heat flux sensors, based on the anomalous Nernst effect (ANE), because of its sizeable uniaxial magnetic anisotropy (K_u) and low saturation magnetization (M_s). We experimentally and theoretically investigated the ANE and anomalous Hall effect in sputter-deposited Mn₄N films. It was revealed that the observed negative anomalous Hall conductivity (σ_{xy}) could be explained by two different coexisting magnetic structures, that is, a dominant magnetic structure with high K_u , contaminated by another structure with negligible K_u , owing to an imperfect degree of order of N. The observed transverse thermoelectric power (S_{ANE}) of +0.5 $\mu\text{V/K}$ at 300 K yielded a transverse thermoelectric

coefficient (α_{xy}) of +0.34 A/(m·K), which was smaller than the value predicted from the first-principles calculation. The interpretation for α_{xy} based on the first-principles calculations led us to conclude that the realization of single magnetic structure with high K_u and optimal adjustment of the Fermi level are promising approaches to enhance S_{ANE} in Mn₄N through the sign reversal of σ_{xy} and the enlargement of α_{xy} up to a theoretical value of 1.77 A/(m·K).

<Main text>

Thermoelectric conversion based on the anomalous Nernst effect (ANE)¹⁾ is an intriguing alternative technology to those based on the conventional Seebeck effect,²⁾ because the transverse thermoelectric power based on the ANE (S_{ANE}) is given in the perpendicular direction with respect to the heat current as shown in the following equation,

$$\mathbf{E}_{ANE} = S_{ANE} \nabla T \times \left(\frac{\mathbf{M}}{|\mathbf{M}|} \right), \quad (1)$$

where \mathbf{E}_{ANE} , \mathbf{M} , and ∇T denote the electric field due to the ANE, magnetization, and temperature gradient, respectively. Owing to these characteristics, a prototype coplanar-type thermopile module has been fabricated using magnetic materials and an enhancement of the serial voltage has been demonstrated.^{3,4)}

One of the most promising applications of the ANE-based coplanar thermopile structure is heat flux sensors. Zhou *et al.* recently fabricated a prototype ANE-based heat flux sensor on a flexible thin polyimide sheet and successfully demonstrated heat flux sensing through ANE.⁵⁾

Although the sensor has the potential to be versatile because of its high flexibility and low thermal resistance, its low sensitivity is the most important disadvantage that needs to be mitigated. To overcome this limitation, magnetic materials with large S_{ANE} are indispensable.⁶⁾ Furthermore, because the magnetization direction must be aligned to the width direction of magnetic wires, even at zero field, low M_s is also an important factor in decreasing the demagnetization field in magnetic wires that causes a reduction of E_{ANE} in the zero-field state.⁵⁾ To stabilize the spontaneous magnetization, high uniaxial magnetic anisotropy (K_u) is also desirable. In recent years, ferromagnetic Heusler alloys, such as Co_2MnGa ⁷⁻⁹⁾ and $\text{Co}_2\text{MnAl}_{0.63}\text{Si}_{0.37}$,¹⁰⁾ have been fabricated that exhibit high S_{ANE} of $\sim 6 \mu\text{V/K}$. However, their high M_s and low K_u are not suitable for a heat flux sensor. In contrast, $0.1\sim 0.5 \mu\text{V/K}$ was reported in Mn_3Sn films, irrespective of its extremely low M_s down to $\sim 10^{-3} \text{ T}$.¹¹⁾ However, its S_{ANE} value is not sufficient for the sensor. Therefore, exploring magnetic materials with high S_{ANE} , low M_s , and high K_u has been of significant importance.

In the present study, we focus on Mn_4N as a promising candidate material with low M_s and high K_u . Mn_4N film has long been known as a Mn-based perpendicular magnetic anisotropy (PMA) ferrimagnetic material with an antiperovskite structure described by the formula ANB_3 , where A and B correspond to Mn(I) at corner sites and Mn(II) at face-centered sites, respectively.^{12,13)} Owing to the ferrimagnetism of Mn_4N , its M_s is much smaller than that in conventional ferromagnets, such as Co-based Heusler alloys, Fe-based alloys, and nitride systems. The high K_u in Mn_4N is also an attractive

feature for usage in ANE-based thermoelectric applications. The Mn_4N films, fabricated by sputtering and molecular-beam epitaxy (MBE) in previous studies, exhibited $M_s \approx 0.1$ T and $K_u \approx 0.1$ MJ/m³.¹⁴⁻

¹⁹⁾ Although the AHE for Mn_4N has been reported,^{17,20)} the ANE and AHE, including the analysis from the perspective of intrinsic mechanism, have not yet been studied.

In this study, we measured both the ANE and AHE of Mn_4N films to analyze the mechanisms of ANE. Our results reveal that Mn_4N is one of the few materials that satisfies the requirements of M_s and K_u for heat flux sensors, while its S_{ANE} is moderate. The first-principles calculations revealed that two different magnetic structures coexist in present Mn_4N films and adjustment of the Fermi level is necessary to enhance the ANE.

Two 20-nm-thick Mn_4N films were grown on single-crystal MgO (001) substrates by reactive nitridation sputtering at substrate temperatures of 400 °C, 450 °C, and 500 °C (referred to as “sample-I,” “sample-II,” and “sample-III,” respectively), and 2 nm thick Al films were then deposited as capping layers. The flow ratio of N_2 to Ar gas was 12 %. Structural analysis was performed using X-ray diffractometry (XRD) with $\text{Cu } K_\alpha$ radiation (SmartLab: Rigaku, Inc.). The magnetic properties were measured via a superconducting quantum interference device vibrating sample magnetometer (SQUID-VSM: Quantum Design, Inc.). The K_u was estimated by $M_s H_k / 2 + M_s^2 / 2 \mu_0$, where the anisotropy field, H_k , is defined as the saturation magnetic field difference between the in-plane and out-of-plane directions. The ANE and AHE were measured by a physical property measurement

system (VersaLab: Quantum Design, Inc.). Rectangular patterned samples with dimensions of $w = 2$ mm and $l = 7$ mm (where w is width and l is length) were prepared via photolithography and Ar-ion milling. The anomalous Hall (Nernst) voltage V_{AHE} (V_{ANE}) was measured in the y -direction by applying I_x (∇T_x) and the external magnetic field, H_z (H_z), as shown in Fig. 1. ∇T_x was strictly measured by an infrared camera with a black body coating on the sample.^{5,10,21)} The Seebeck coefficients of the films (S_{SE}) were measured by using a Seebeck coefficient or electric resistance measurement system (ZEM-3: ADVANCE RIKO, Inc.) equipped with R-type thermocouples.

In the theoretical calculation of the anomalous Hall conductivity (σ_{xy}) and the transverse thermoelectric coefficient (α_{xy}), we combined the first-principles calculations and the Boltzmann transport theory. The electronic structure of the stoichiometric Mn_4N was first calculated using the full-potential linearized augmented plane-wave method, including the effect of spin-orbit interactions, which was implemented in the WIEN2K program.²²⁾ The lattice constants of the unit cell were fixed at $a = 3.87726$ Å and $c = 3.83974$ Å ($c/a = 0.99$), which were the experimental values evaluated from the in-plane and out-of-plane XRD profiles. The self-consistent-field calculation using $24 \times 24 \times 25$ k points yielded both magnetic structures type-A and type-B. For the obtained electronic structures, we calculated σ_{xy} and α_{xy} employing the same method as that used in our previous work.⁹⁾ In the calculation of α_{xy} , the temperature T was set to 300 K. We used $89 \times 89 \times 90$ k points for the Brillouin-zone integration, ensuring good convergence for σ_{xy} and α_{xy} .

Figure 2 shows the out-of-plane XRD profiles for sample-I, II, and III. As shown by dashed lines, the peak intensities were fitted with pseudo-Voigt functions.²³⁾ The diffraction peaks at $2\theta/\omega \approx 23^\circ$ and 47° correspond to the (001) superlattice and (002) fundamental peaks of the Mn_4N crystals, respectively. The degree of order (S) of fabricated Mn_4N epitaxial films was estimated using the integral diffraction intensity of the Mn_4N (001) and (002) peaks: $S = \sqrt{\frac{I_{001}^{\text{obs}}/I_{002}^{\text{obs}}}{I_{001}^{\text{cal}}/I_{002}^{\text{cal}}}}$, where I_{hkl}^{obs} and I_{hkl}^{cal} correspond to the integral intensities of the peaks, originating from (hkl) planes. These intensities were obtained from the pseudo-Voigt function fitting results and calculations, respectively (see Supplementary Material). The resultant S for sample-I, II, and III were estimated to be 0.6, 0.7, and 0.7, respectively, which were found to be relatively close to the film, deposited by MBE and sputtering techniques.^{17,24)} Although an Mn_4N unit cell, with a body-centered N, is the most stable phase, there are 12 possible equivalent sites for N atoms, similar to that in Fe_4N .²⁵⁾ Therefore, the S in this study represents the degree of order for both—N site ordering and its deficiency. Figure 2(b), 2(c), and 2(d) show the magnetization curves for sample-I, II, and III, respectively, where H was swept along the [100] and [001] directions of the Mn_4N crystals. Comparing the two curves in different directions, the magnetic easy-axis was found to point in the [001] direction; that is, sample-II showed sizeable PMA ($K_u \approx 0.13 \text{ MJ/m}^3$). The value of $\mu_0 M_s$ was measured to be 100 mT, comparable to that of Mn_4N films fabricated by sputtering and MBE.¹⁴⁻¹⁹⁾ In case of sample-I and III, the two magnetization curves, with $H \parallel [100]$ and [001], showed similar magnetization process, indicating negligible PMA ($K_u \approx 0.003$

and 0.001 MJ/m³ for sample-I and -III, respectively). The value of $\mu_0 M_s$ was decreased to 90 and 60 mT for sample-I and -III, respectively. These crystal structure and magnetization results show that 450 °C is an optimum substrate temperature for Mn₄N to yield high PMA with higher S , in this study.

From the linear response equation, S_{ANE} is given by⁹⁾

$$S_{ANE} = \rho_{xx}\alpha_{xy} + \rho_{xy}\alpha_{xx} , \quad (2)$$

where $\rho_{xx(xy)}$ and α_{xx} denote the longitudinal (anomalous Hall) resistivity and longitudinal thermoelectric coefficients, respectively. The second term of Eq. (2) corresponds to the contribution of the AHE to the ANE; therefore, the measurement of ρ_{xy} is necessary to study the origin of S_{ANE} . Figure 3(a) shows the ρ_{xy} curves for sample-I, II, and III as functions of H_z at 300 K, indicating hysteresis similar to the $M-H$ curves shown in Fig. 2(b), 2(c), and 2(d). Figure 3(b) and 3(c) show the measurement temperature (T) dependence of ρ_{xy} and ρ_{xx} , respectively. ρ_{xx} decreased with decreasing T , suggesting metallic properties in the present three films. Figure 3(d) shows the T dependence of σ_{xy} , estimated using the following formula:⁹⁾

$$\sigma_{xy} = -\frac{\rho_{xy}}{\rho_{xy}^2 + \rho_{xx}^2} . \quad (3)$$

σ_{xy} was negative for both films: $\sigma_{xy} \approx -50, -80$, and -78 S/cm at 300 K, and $\sigma_{xy} \approx -10, -100$, and -98 S/cm at 4 K for sample-I, II, and III, respectively. The inset of Fig. 3(d) represents the $\sigma_{xy}-\sigma_{xx}$ relationship for the three samples. σ_{xy} for sample-II and III remains constant in contrast to that of sample-I, which qualitatively suggests that sample-II and III contain stronger intrinsic contribution of

AHE, compared with sample-I.

Figure 4(a) shows the H_z dependence of V_{ANE} normalized by w and ∇T_x for the three samples. To evaluate S_{ANE} , V_{ANE} was measured under different ∇T_x and the intrinsic component of ANE was evaluated by linear curve fitting in the high $\mu_0 H_z$ region and taking the intercept at zero field. The inset shows the plot of the dependence of V_{ANE}/w , obtained by the linear fitting on ∇T_x for sample-II; the slope of least-squares fitting yields an averaged S_{ANE} of 0.50 $\mu\text{V/K}$. The α_{xy} for sample-II was estimated to be 0.34 A/(m·K), using Eq. (2), with the measured values of S_{ANE} , $\rho_{xx(xy)}$, and longitudinal thermoelectric coefficient, $\alpha_{xx} (= S_{\text{SE}}/\rho_{xx})$. In contrast, the α_{xy} for sample-I and II were estimated to be 0.16 and 0.21 A/(m·K), respectively. Figure 4(b) shows the reported S_{ANE} for various materials plotted against M_s . Based on the analysis of the required $\mu_0 M_s$ and S_{ANE} for an ANE-based heat flux sensor, reported by Zhou *et al.*,⁵⁾ $\mu_0 M_s < 0.2$ and $S_{\text{ANE}} > 10 \mu\text{V/K}$ are required to suppress the demagnetization field to less than 0.1 T and the sensitivity to 10 $\mu\text{V}/(\text{Wm}^{-2})$ in a $1 \times 1 \text{ cm}^2$ size sensor with 10 μm as both height and the width of the magnetic wires. Therefore, this required range is highlighted in Fig. 4(b). Although the observed S_{ANE} for sample-II [marked by a star in Fig. 4(b)] does not reach the target region showing the necessary values for heat flux sensors, one can notice that Mn_4N is one of the few materials with small M_s that satisfies this target and shows a relatively high S_{ANE} value, as compared to other materials, such as Mn_3Sn ¹¹⁾ and $\text{DO}_{22}\text{-Mn}_3\text{Ga}$.²⁶⁾

The first-principles calculations for σ_{xy} and α_{xy} were carried out from the perspective of

intrinsic mechanism to understand the origin of observed AHE and ANE in the Mn_4N films. Two possible collinear magnetic structures for Mn_4N were investigated in our previous study (see Fig. 1 for the magnetic structures): “type-A,” in which the magnetic moments of Mn(I) and Mn(II) point in opposite directions, giving tiny M_s (≈ 7.9 mT) and negligible K_u ; and “type-B,” in which the magnetic moments couple parallel to each other, within the ab -plane, and alternately, along the c -direction, giving low M_s (≈ 0.18 T) and high K_u (≈ 4 MJ/m³).¹⁹⁾ Type-B is energetically more stable, compared with type-A, when $S = 1$.¹⁹⁾ Because $\mu_0 M_s$ was measured to be 100 mT and a clear PMA ($K_u \approx 0.13$ MJ/m³) was observed, we inferred that type-B magnetic structure was dominant in sample-II. Therefore, first, the calculation of σ_{xy} with type-B was performed [solid line in Fig. 5(a)]. It was revealed that the calculated σ_{xy} of 573 S/cm at the Fermi level ($\mu = 0$ eV) was inconsistent with the experimental value of -100 S/cm at 4 K. Such a large discrepancy motivated us to calculate σ_{xy} with type-A structure [dashed line in Fig. 5(a)]. As a result, we found a negative σ_{xy} at the Fermi level ($\sigma_{xy} = -500$ S/cm), which agreed with the sign of the experimental value, although its magnitude still showed a discrepancy. However, notably, our previous study showed tiny M_s and negligible K_u for the type-A structure,¹⁹⁾ which indicates that type-A magnetic structure cannot be dominant in sample-II. These results imply that the main magnetic structure for sample-II is type-B; however, it is contaminated by a certain amount of type-A, whose contribution to AHE is large enough to reverse the sign of σ_{xy} to negative in sample-II. Although the cause of type-A contamination is not fully understood,

imperfect S should be considered as a probable reason for such contamination. Our previous investigation revealed that $S = 1$ can contribute towards forming type-B rather than type-A due to the energy stability of the magnetic structure.¹⁹⁾ Thus, we can infer that type-A—a second stable magnetic structure—possibly appears when S deviates from 1. In contrast to our samples, Kabara *et al.* measured positive σ_{xy} at 4 K for 100 nm thick Mn_4N films, the sign of which agreed with that for type-B.²⁷⁾ Such a consistency can be attributed to the enhanced S (≈ 0.85) due to the large layer thickness,¹⁷⁾ and the contribution from type-A, if any, may be veiled by that from type-B. As for the experimental results shown in Fig. 2(b) and 2(c), the M_s and K_u for sample-I ($S = 0.6$) were less than those for sample-II ($S = 0.7$), which could be related to the higher contamination of type-A due to lower S in sample-I. However, the M_s and K_u for sample-III were smaller than those for sample-II, as shown in Fig. 2(c) and 2(d), in spite of the similar, S , i.e., $S = 0.7$. Although these magnetic properties can be also attributed to the contamination of type-A, additional mechanisms are considered because the coercivity for sample-III clearly increased, as compared to sample-II. We observed island-like surface morphology and/or large surface roughness in sample-III (See supplementary material), via atomic force microscopy (AFM). These structural characteristics are responsible for the magnetic properties observed in sample-III through pinning of domain walls, as reported in the case of Co/Ni multilayer.²⁸⁾ On the other hand, the negatively smaller σ_{xy} for sample-I, compared with those for sample-II and III, cannot be explained by the higher type-A contamination, because type-A contribution decreases the

entire σ_{xy} . We can see a steep change in the calculated σ_{xy} around the Fermi level in both type-A and – B structures, suggesting that σ_{xy} is sensitive to μ [Fig. 5(a)]. For example, the change in μ , within ± 0.05 eV, results in a large variation width, of ~ 400 S/cm, for both magnetic structures. Therefore, the S -dependent shift in the Fermi level can be another cause of the negatively smaller σ_{xy} for sample-I, as compared to those of sample-I and III.

Figure 5(b) shows the μ dependence of α_{xy} , where T is set to 300 K. At the Fermi level, $\mu = 0$, $\alpha_{xy} = 1.66$ (1.77) A/(m·K) for type-A (type-B). Comparing $|\alpha_{xy}|$ for the representative materials, we obtain $|\alpha_{xy}| = 4$ for Co₂MnGa,⁷⁾ 1.2 for FeGa,²¹⁾ 1.1 for MnSi,²⁹⁾ 0.6 for SrRuO₃,³⁰⁾ and 0.3 for Mn₃Sn¹¹⁾ from the experiments, and 0.9 for FePt,³¹⁾ 0.52 for Co,³¹⁾ and 0.21 for Fe³¹⁾ from the calculations [all in units of A/(m·K)]. From these values, one can find that the calculated α_{xy} for Mn₄N, based on intrinsic origins, is sufficiently high. Therefore, Mn₄N can be a promising material for ANE. Unlike σ_{xy} , high α_{xy} with a positive sign was predicted for both magnetic structures, which is beneficial for the enhancement of S_{ANE} , even in the case of type-A contamination. However, the measured α_{xy} was one order of magnitude smaller than that from the calculation. One possible explanation is the shift of Fermi level from the theoretically obtained value as well as its effect on σ_{xy} , because the peak around the Fermi level is remarkably sharp [Fig. 5(b)]. For example, the even small change in μ with ± 0.05 eV provides a large variation width of ~ 2.7 (~ 1.8) A/(m·K) for type-A (type-B). The S in Mn₄N is related to the site ordering of N as well as the N deficiency (shown in Fig. 2); therefore, less S

corresponds to a decrease in the number of electrons in the Mn_4N unit cell. This can be responsible for the shift in the Fermi level, on the basis of the rigid-band model.³²⁾ In addition, quantifying the extrinsic contributions, such as skew-scattering and/or side-jump, may be necessary for explaining the discrepancy,³³⁾ although the nearly constant $\sigma_{xx} \approx 5 \times 10^3 (\Omega \text{ cm})^{-1}$ for sample-II and III are categorized into the intrinsic regime, based on the σ_{xy} - σ_{xx} relationship,³⁴⁾ as shown in the inset of Fig. 3(d).

Next, we address how to boost the ANE in Mn_4N . Equation (3) states that S_{ANE} decreases and increases when the signs of the first ($\rho_{xx}\alpha_{xy}$) and second ($\rho_{xy}\alpha_{xx}$) terms are opposite and same, respectively. In the case of the present Mn_4N films, as shown in Table I, the resultant S_{ANE} lost due to the negative sign of $\rho_{xy}\alpha_{xx}$. In addition, the enhanced α_{xy} , which is realized via modulation of the Fermi level, is also necessary to boost S_{ANE} for a Mn_4N system. To modulate the Fermi level and obtain positive $\rho_{xy}\alpha_{xx}$, realizing Mn_4N with ideal type-B and no or negligible contamination from type-A, via improved S , is a promising approach. Furthermore, the substitution of a third element, such as Ni, into Mn_4N may be another interesting approach for enhancing S_{ANE} as well as reducing M_s . This is because the sign reversal of AHE occurs with a Ni content of ~ 5 at.%.³⁵⁾ Such a small Ni content retains the antiperovskite crystal structure,³⁵⁾ suggesting a similar band structure and modulation of the Fermi level, based on the rigid-band model.³²⁾ Therefore, the results of the present study can open a pathway for fabricating Mn_4N -based materials to develop heat flux sensors.

Table I. Summary of coefficients related to the ANE and AHE for Mn_4N .

	Experiment			Calculation	
	Sample-I (400 °C)	Sample-II (450 °C)	Sample-III (500 °C)	Type-A	Type-B
$\mu_0 M_s$ (mT)	88	100	60	7.9 (0 K) ¹⁹⁾	180 (0 K) ¹⁹⁾
K_u (MJ/m ³)	0.003	0.13	0.001	~0 (0 K)	4 (0 K)
ρ_{xx} ($\mu\Omega$ cm)	240	190	230		
ρ_{xy} ($\mu\Omega$ cm)	2.6	2.8	3.8		
σ_{xy} (S/cm)	-50 -10 (4 K)	-80 -100 (4 K)	-78 -98 (4 K)	-573 (0 K)	500 (0 K)
θ_{AHE} (%)	1.1	1.5	1.65		
S_{SE} ($\mu\text{V/K}$)	-14	-9.7	-11.8		
$S_{\text{AHE}} = S_{\text{SE}}$	-0.15	-0.15	-0.19		
$\tan \theta_{\text{AHE}}$ ($\mu\text{V/K}$)					
α_{xx} [A/(m·K)]	-5.7	-5.1	-5.0		
α_{xy} [A/(m·K)]	0.16	0.34	0.21	1.77	1.66
$\rho_{xx}\alpha_{xy}$ ($\mu\text{V/K}$)	0.38	0.65	0.49		
$\rho_{xy}\alpha_{xx}$ ($\mu\text{V/K}$)	-0.15	-0.15	-0.19		
S_{ANE} ($\mu\text{V/K}$)	0.23	0.50	0.30		

In summary, we studied the AHE and ANE for sputter-deposited 20-nm-thick ferrimagnetic Mn_4N films. S_{ANE} was measured to be $0.50 \mu\text{V/K}$, which is the maximum value at 300 K, demonstrating that Mn_4N is one of the few materials that shows relatively large S_{ANE} with low M_s and high K_u . The Mn_4N film characteristics, revealed via the first-principles calculations in this study, are: i) the possible magnetic structure of the film may be type-B; however, type-A, with small M_s and negligible K_u , may be partly included; ii) S_{ANE} decreases because of the imperfect S , thereby reducing α_{xy} and causing the negative sign of the AHE component. To reach the target of heat flux sensors, further enhancement of S_{ANE} of Mn_4N is critical. Useful approaches to be considered are: obtaining a positive σ_{xy} and enhanced α_{xy} via the Fermi-level tuning and improving S , leading to type-B magnetic structure. Thus, the present study provides insights into the fundamentals of the transverse transport properties of Mn-based nitride systems.

<Supplementary Material>

See supplementary material for details on estimating the degree of order of Mn_4N and the surface morphologies, observed via AFM.

<Acknowledgement>

This work was supported by JSPS KANENHI via grant no. 19K04499, 19K21954, 18H03787, and 16H06332; PRESTO from the Japan Science and Technology Agency (No. JPMJPR17R5); and NEDO “Mitou challenge 2050” (Grant No. P14004). The authors thank B. Masaoka for his technical support.

Part of this work was carried out under the Cooperative Research Project Program of the RIEC, Tohoku University.

<Data Availability>

The data that support the findings of this study are available from the corresponding author upon reasonable request.

<References>

- [1] W. Nernst, Ann. Phys. **267**, 760 (1887).
- [2] H. J. Goldsmid, Proc. Phys. Soc. **71**, 633 (1958).
- [3] Y. Sakuraba, K. Hasegawa, M. Mizuguchi, T. Kubota, S. Mizukami, T. Miyazaki, and K. Takanashi, Appl. Phys. Express **6**, 033003 (2013).
- [4] Y. Sakuraba, Scr. Mater. **111**, 29 (2016).
- [5] W. Zhou and Y. Sakuraba, Appl. Phys. Express **13**, 043001 (2020).
- [6] A. Sakai, S. Minami, T. Koretsune, T. Chen, T. Higo, Y. Wang, T. Nomoto, M. Hirayama, S. Miwa, D. N. Hamane, F. Ishii, R. Arita, and S. Nakatsuji, Nature **581**, 53 (2020).
- [7] A. Sakai, Y. P. Mizuta, A. A. Nugroho, R. Sihombing, T. Koretsune, M. Suzuki, N. Takemori, R. Ishii, D. N. Hamane, R. Arita, P. Goswami, and S. Nakatsuji, Nature Physics **14**, 1119 (2018).
- [8] S. N. Guin, K. Manna, J. Noky, S. J. Watzman, C. Fu, N. Kumar, W. Schnelle, C. Shekhar, Y. Sun, J. Gooth, and C. Felser, NPG Asia Mater. **11**, 16 (2019).
- [9] K. Sumida, Y. Sakuraba, K. Masuda, T. Kono, M. Kakoki, K. Goto, W. Zhou, K. Miyamoto, Y.

Miura, T. Okuda & A. Kimura, *Comms. Mater.* **1**, 89 (2020)

- [10] Y. Sakuraba, K. Hyodo, A. Sakuma, and S. Mitani, *Phys. Rev. B* **101**, 134407 (2020).
- [11] M. Ikhlas, T. Tomita, T. Koretsune, M. Suzuki, D. N. Hamane, R. Arita, Y. Otani, and S. Nakatsuji, *Nature Physics* **13**, 1085 (2017).
- [12] W. J. Takei, G. Shirane, and B. C. Frazer, *Phys. Rev.* **119**, 1893 (1960).
- [13] W. J. Takei, R. R. Heikes, and G. Shirane, *Phys. Rev.* **125**, 1893 (1962).
- [14] S. Nakagawa and M. Naoe, *J. Appl. Phys.* **75**, 6568 (1994).
- [15] K. M. Ching, W. D. Chang, T. S. Chin, J. G. Duh, and H. C. Ku, *J. Appl. Phys.* **76**, 6582 (1994).
- [16] Y. Yasutomi, K. Ito, T. Sanai, K. Toko, and T. Suemasu, *J. Appl. Phys.* **115**, 17A935 (2014).
- [17] K. Kabara, and M. Tsunoda, *J. Appl. Phys.* **117**, 17B512 (2015).
- [18] K. Ito, Y. Yasutomi, K. Kabara, T. Gushi, S. Higashikozono, K. Toko, M. Tsunoda, and T. Suemasu, *AIP Advances* **6**, 056201 (2016).
- [19] S. Isogami, K. Masuda, and Y. Miura, *Phys. Rev. Mater.* **4**, 014406 (2020).
- [20] X. Shen, A. Chikamatsu, K. Shigematsu, Y. Hirose, T. Fukumura, and T. Hasegawa, *Appl.*

Phys. Lett. **105**, 072410 (2014).

[21] H. Nakayama, K. Masuda, J. Wang, A. Miura, K. Uchida, M. Murata, and Y. Sakuraba, Phys.

Rev. Mater. **3**, 114412 (2019).

[22] P. Blaha, K. Schwarz, G. K. H. Madsen, D. Kvasnicka, J. Luitz, R. Laskowski, F. Tran, L. D.

Marks, <http://www.wien2k.at>.

[23] W. I. F. David, J. Appl. Cryst. **19**, 63 (1986).

[24] S. Isogami, A. Anzai, T. Gushi, T. Komori, and T. Suemasu, Jpn. J. Appl. Phys. **57**, 120305

(2018).

[25] K. Kabara, M. Tsunoda, and S. Kokado, Appl. Phys. Express **7**, 063003 (2014).

[26] K. Hasegawa, M. Mizuguchi, Y. Sakuraba, T. Kamada, T. Kojima, T. Kubota, S. Mizukami,

T. Miyazaki, and K. Takanashi, Appl. Phys. Lett. **106**, 252405 (2015).

[27] K. Kabara, M. Tsunoda, and S. Kokado, AIP Advances **7**, 056416 (2017).

[28] N. R. L. Hone, R. Thanhoffer, V. Neu, R. Schäfer, M. Arora, R. Hübner, D. Suess, D.M. Broun,

and E. Girt, J. Magn. Magn. Mater. **441**, 283 (2017).

- [29] Y. Hirokane, Y. Tomioka, Y. Imai, A. Maeda, and Y. Onose, *Phys. Rev. B* **93**, 014436 (2016).
- [30] T. Miyasato, N. Abe, T. Fujii, A. Asamitsu, S. Onoda, Y. Onose, N. Nagaosa, and Y. Tokura, *Phys. Rev. Lett.* **99**, 086602 (2007).
- [31] J. Weischenberg, F. Freimuth, S. Blugel, and Y. Mokrousov, *Phys. Rev. B* **87**, 060406 (2013).
- [32] E. A. Stem, *Phys. Rev.* **157**, 544 (1967).
- [33] M. Meng, S. X. Wu, L. Z. Ren, W. Q. Zhou, Y. J. Wang, G. L. Wang, and S. W. Li, *Appl. Phys. Lett.* **106**, 032407 (2015).
- [34] S. Onoda, N. Sugimoto, and N. Nagaosa, *Phys. Rev. B* **77**, 165103 (2008).
- [35] T. Komori, T. Gushi, A. Anzai, L. Vila, J. P. Attané, S. Pizzini, J. Vogel, S. Isogami, K. Toko, and T. Suemasu, *J. Appl. Phys.* **125**, 213902 (2019).
- [36] A. Miura, K. Masuda, T. Hirai, R. Iguchi, T. Seki, Y. Miura, H. Tsuchiura, K. Takanashi, and K. Uchida, *Appl. Phys. Lett.* **117**, 082408 (2020).
- [37] S. Isogami, K. Takanashi, and M. Mizuguchi, *Appl. Phys. Express* **10**, 073005 (2017).

<Figure captions>

Figure 1. Measurement configuration of anomalous Nernst voltage (V_{ANE}) and anomalous Hall voltage (V_{AHE}) for the MgO substrate/Mn₄N (20 nm)/Al (2 nm). The right schematic illustration represents the crystal structure of the Mn₄N unit cell and the magnetic structures, type-A and type-B.

Figure 2. (a) Out-of-plane X-ray diffraction profiles of sample-I (substrate temperature, $T_{\text{sub}} = 400$ °C), sample-II (450 °C), and sample-III (500 °C). The dashed lines indicate the peak fitting to evaluate the degree of order of N (S). (c, d, e) Magnetization curves of sample-I, sample-II, and sample-III.

Figure 3. (a) Representative anomalous Hall resistivity (ρ_{xy}) as a function of the applied magnetic field along z -direction (H_z) at 300 K. (b, c, d) Dependence of anomalous Hall resistivity (ρ_{xy}) (b), longitudinal resistivity (ρ_{xx}) (c), and anomalous Hall conductivity (σ_{xy}) (d) on measurement temperature (T). The inset represents the plot of $|\sigma_{xy}|$ vs σ_{xx} .

Figure 4. (a) Representative anomalous Nernst voltage (V_{ANE}) at 300 K as a function of the applied magnetic field, pointing in the z -direction (H_z). The inset represents saturated V_{ANE} as a function of temperature gradient (∇T_x). The solid line shows the least-squares fitting with a linear function. The corresponding slope yields $V_{ANE}/(w \cdot \nabla T_x)$. (b) Thermoelectric power (S_{ANE}), for various materials,

plotted against saturation magnetization ($\mu_0 M_s$). Red color represents the target values for heat flux sensors.

Figure 5. (a,b) Calculated anomalous Hall conductivity (σ_{xy}) (a) and transverse thermoelectric coefficient (α_{xy}) (b) as functions of chemical potential (μ) for the Mn_4N unit cell. The dashed and solid lines represent the results for magnetic structure type-A and type-B, respectively.

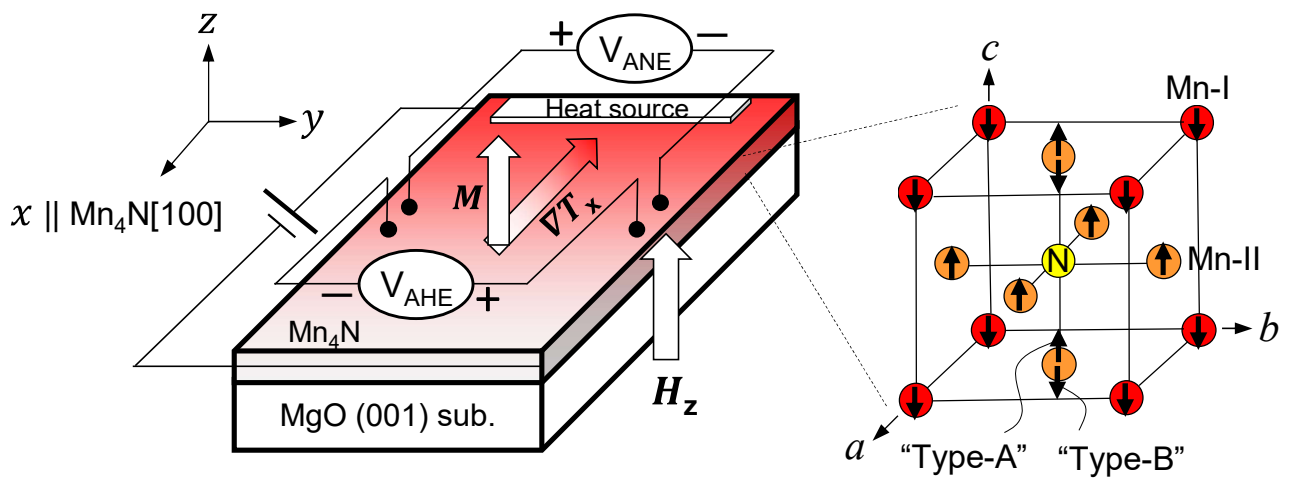


Fig. 1

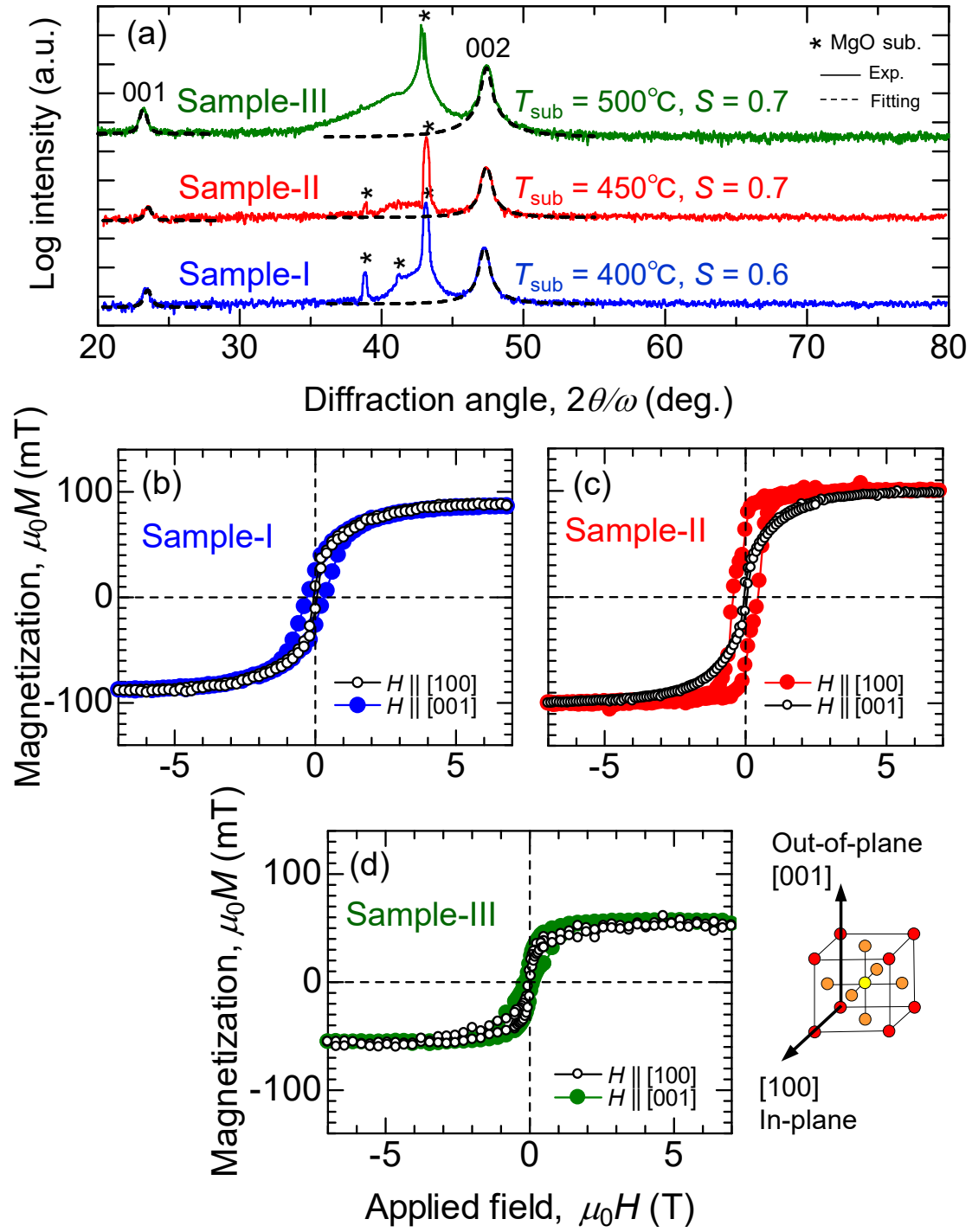


Fig. 2

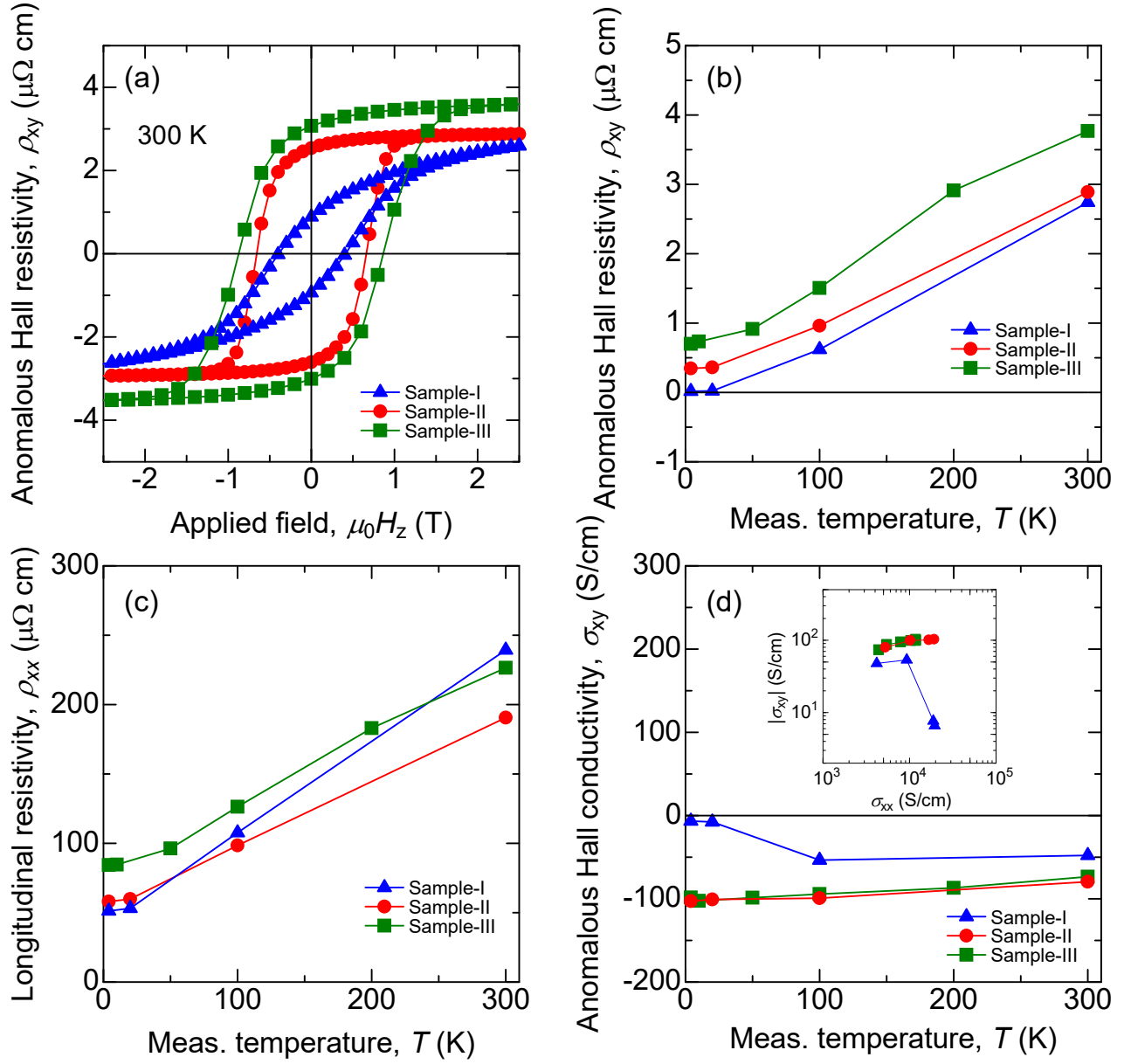


Fig. 3

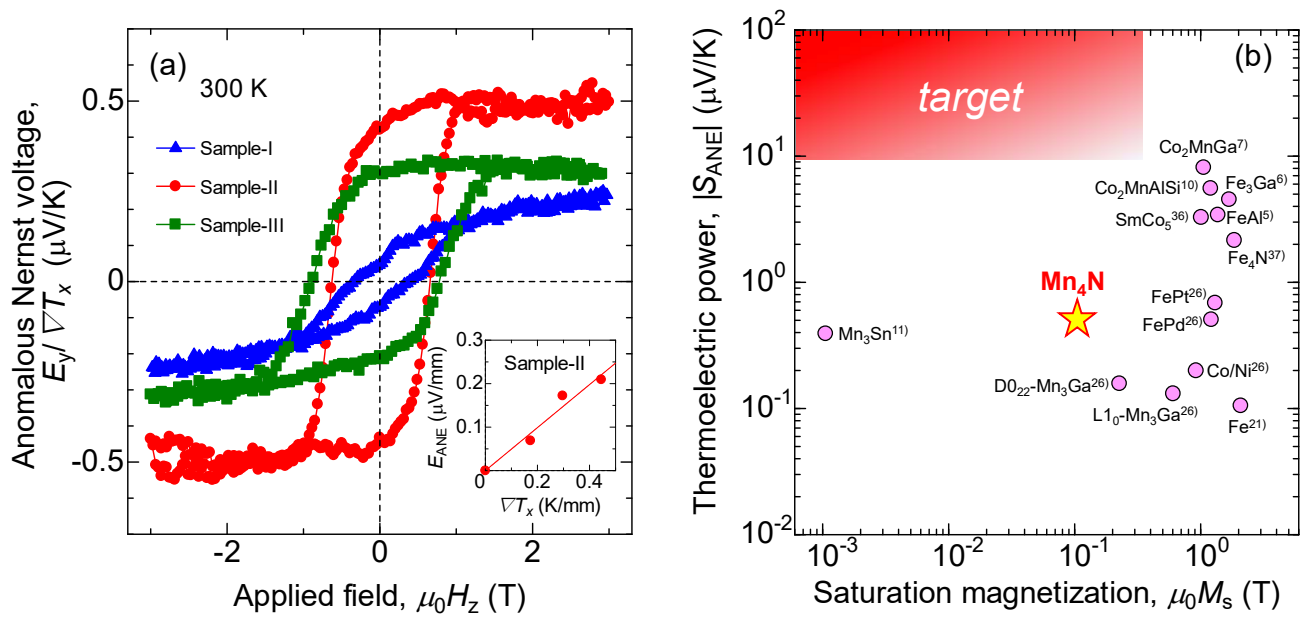


Fig. 4

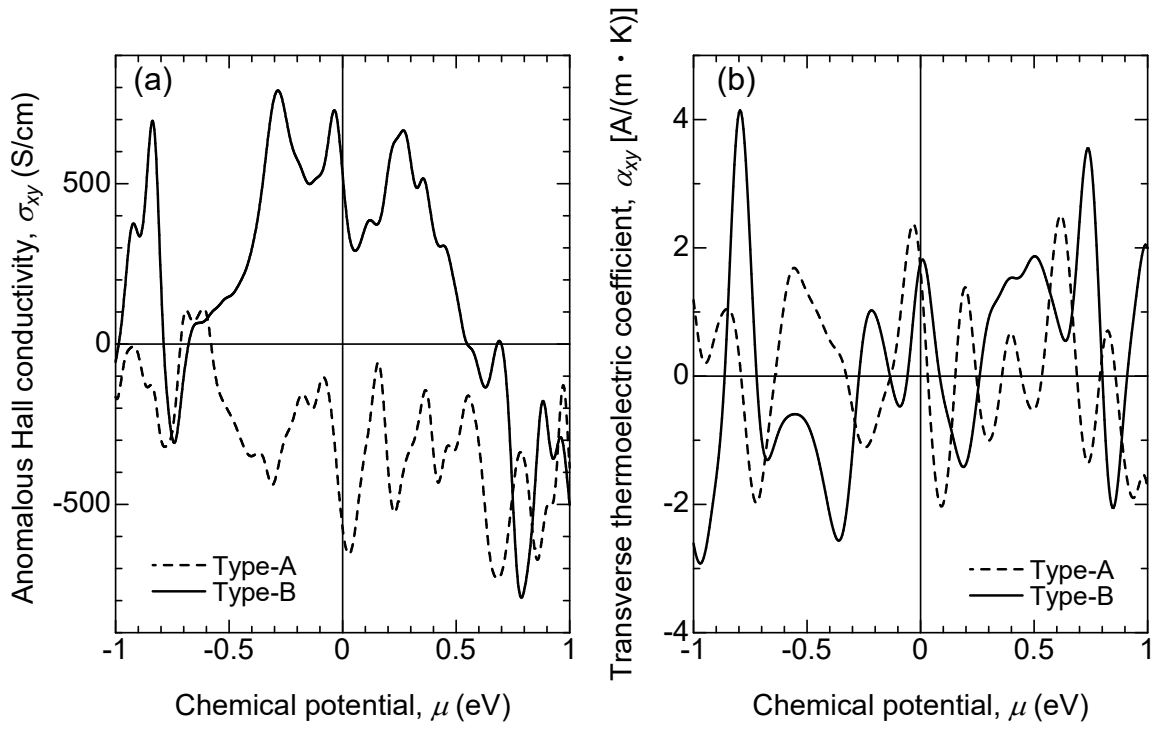


Fig. 5

Supplementary Material

Anomalous Hall and Nernst effects in ferrimagnetic Mn₄N films: Possible interpretations and prospects for enhancement

Shinji Isogami^{1a)}, Keisuke Masuda¹, Yoshio Miura¹, Rajamanickam Nagalingam¹, and
Yuya Sakuraba^{1,2}

¹ National Institute for Materials Science, Tsukuba 305-0047, Japan

² PRESTO, Japan Science and technology Agency, Saitama 332-0012, Japan

a) isogami.shinji@nims.go.jp

S1. Estimation of degree of order (S)

From the XRD profiles, the degree of order (S) of the fabricated Mn₄N epitaxial films was estimated as:

$$S = \sqrt{\frac{I_{001}^{\text{obs}}/I_{002}^{\text{obs}}}{I_{001}^{\text{cal}}/I_{002}^{\text{cal}}}} , \quad (\text{S1})$$

$$I_{hkl}^{\text{cal}} = A \cdot |F_{hkl}|^2 \cdot LP , \quad (\text{S2})$$

where

$$A = \frac{1}{2\mu} (1 - e^{-2\mu t / \sin \theta}) , \quad (\text{S3})$$

$$LP = \frac{1 + \cos^2(2\theta) \cos^2(2\theta_M)}{\sin(2\theta) \{1 + (\cos^2 \theta_M)\}} . \quad (\text{S4})$$

I_{hkl}^{obs} and I_{hkl}^{cal} correspond to the integral peak intensities of peaks from (hkl) planes, which are obtained by the pseudo-Voigt function fitting results and calculations, respectively. A and LP correspond to the absorption factor with line absorption coefficient (μ) and film thickness (t), the Lorenz polarization factor with Bragg angle (θ_M) of the monochromator $\text{Ge}(220) = 22.65^\circ$, respectively. The structure factor (F_{hkl}) of Mn₄N was estimated using:

$$F_{hkl} = f_{\text{Mn}} \{1 + (-1)^{h+k} + (-1)^{k+l} + (-1)^{l+h}\} + f_{\text{N}} (-1)^{h+k+l} , \quad (\text{S5})$$

where f represents the atomic scattering factor.

S2. Surface morphology of the 20-nm-thick Mn_4N film with higher substrate temperature ($T_{\text{sub}} = 500^\circ\text{C}$)

Figure S1 shows a plot of the surface roughness (R_a) as a function of the substrate temperature (T_{sub}) for the stacked sample: MgO substrate// Mn_4N (20 nm)/Al (2 nm). R_a shows similar values at $T_{\text{sub}} = 400^\circ\text{C}$ and 450°C ; however, it increases by 50 % at $T_{\text{sub}} = 500^\circ\text{C}$. The AFM images show that island-like grains appear at $T_{\text{sub}} = 500^\circ\text{C}$, which may be responsible for the increased R_a .

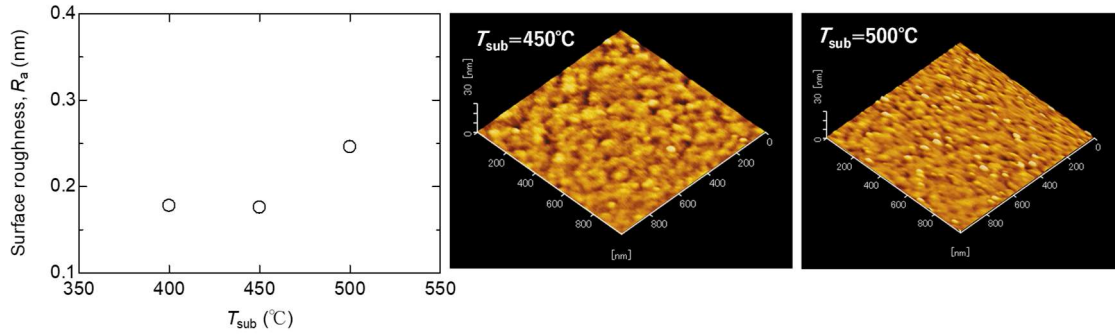


Figure S1 Surface roughness (R_a) as a function of the substrate temperature (T_{sub}) for the stacking—MgO substrate// Mn_4N (20 nm)/Al (2 nm). Both the surface morphologies were observed via AFM with $1\ \mu\text{m} \times 1\ \mu\text{m}$ in dimension.